EUROFUSION WPJET1-PR(16) 14283

P Buratti et al.

Diagnostic application of magnetic islands rotation in JET

Preprint of Paper to be submitted for publication in
Nuclear Fusion

This work has been carried out within the framework of the EUROfusion Consortium and has received funding from the Euratom research and training programme 2014-2018 under grant agreement No 633053. The views and opinions expressed herein do not necessarily reflect those of the European Commission.

Diagnostic application of magnetic islands rotation in JET

P. Buratti[1], E. Alessi[2], M. Baruzzo[3], A. Casolari[1,4], E. Giovannozzi[1], C. Giroud[5], N. Hawkes[5], S. Menmuir[5], G. Pucella[1] and JET Contributors*

EUROfusion Consortium, JET, Culham Science Centre, Abingdon, OX14 3DB, UK

[1]Unità Tecnica Fusione, C.R. ENEA Frascati, CP65, 00044 Frascati, Italy,

[2]IFP-CNR Milano, Italy,

[3]RFX, Corso Stati Uniti 4, Padova, Italy,

[4]Dipartimento di Fisica "Enrico Fermi", Università di Pisa, Largo B. Pontecorvo 3, I-56127 Pisa, Italy

[5]EURATOM/CCFE Fusion Association, Culham Science Centre, Abingdon, OX14 3DB, UK,

**See the Appendix of F. Romanelli et al., Proceedings of the 25th IAEA Fusion Energy Conference 2014, Saint Petersburg, Russia*

Abstract

Measurements of the propagation frequency of magnetic islands in JET are compared with diamagnetic drift frequencies, in view of a possible diagnostic application to the determination of markers for the safety factor profile. Statistical analysis is performed for a database including many well-diagnosed plasma discharges. Propagation in the plasma frame, i.e. with subtracted **E**×**B** Doppler shift, results to be in the ion diamagnetic drift direction, with values ranging from 0.8 (for islands at the $q = 2$ resonant surface) to 1.8 (for more internal islands) times the ion diamagnetic drift frequency. The diagnostic potential of the assumption of island propagation at exactly the ion diamagnetic frequency is scrutinised. Rational-q locations obtained on the basis of this assumption are compared with the ones measured by equilibrium reconstruction including motional Stark effect measurements as constraints. Systematic shifts and standard deviations are determined for islands with (poloidal, toroidal) periodicity indexes of (2, 1), (3, 2), (4, 3) and (5, 3) and possible diagnostic applications are indicated.

1. Introduction

The propagation of coherent magnetic structures is a fundamental problem of plasma physics [1, 2], with relevant implications for magnetic islands stability in tokamaks [3, 4] and for diagnostic applications [5]. The development of magnetic islands by tearing and reconnection of field lines has attracted a great deal of interest because of its effects on plasma confinement

and safety, in particular at high plasma pressure, as reviewed in [6, 7], and for the risk of disruption associated with large islands. Magnetic reconnection locally breaks the axisymmetric topology of flux surfaces enveloping a single circular axis, and secondary helical axes appear, surrounded by isolated magnetic surfaces. Diffusive cross-field transport is short-circuited across magnetic islands by flows along reconnected field lines. Sufficiently large multiple chains of magnetic islands with different helicity can even result in global braiding of field lines, leading to plasma disruption.

One basic question is how is the island phase velocity related to the flows of ion and electron plasma species. This is a relevant issue, as velocity differences determine energy and momentum exchange between the magnetic island and the plasma. In particular, island propagation with respect to the ion fluid gives rise to the so called polarisation current [4], which, depending on its sign, can enforce or damp the island, while propagation with respect to electrons can generate momentum-carrying plasma waves [8].

Theoretical studies based on non-linear drift models predicted propagation with the electron fluid for small islands [9] and with the ion fluid in the limit of large islands [10]. The dependence on island size is complicated as several competing effects are present, in particular sound waves propagation and flow damping [10]. The theoretical development is still evolving and a complete theory of island propagation to compare to experiments is not available at present.

Frequencies of magnetic signals have been compared with the ion and electron diamagnetic frequencies ($\omega_{*\mathrm{i}}$ and $\omega_{*\mathrm{e}}$) in experimental investigations of island propagation [4, 11]. In ref [4], frequencies in the plasma frame (the one with zero $\mathbf{E}\times\mathbf{B}$ velocity) of islands with different (*m, n*) pairs were compared with the ion diamagnetic frequency at the respective $q=m/n$ resonant surfaces. The comparison is challenging because the $\mathbf{E}\times\mathbf{B}$ Doppler shift (ω_E) between the laboratory and the plasma frame is typically much larger than the diamagnetic frequencies. Propagation in the ion drift direction (i.e. frequency with the same sign as the ion diamagnetic frequency) was found, with relative values $\omega/\omega_{*\mathrm{i}}$ varying from about 0.5 for (2, 1) islands (far from the plasma axis) to 1.7 for more internal (5, 4) and (4, 3) islands. A few cases (three at most) were considered in [4] for each (*m, n*) pair and error bars were estimated a priori. A comparison involving a wide database was done in ref. [11] for (2, 1) islands, confirming propagation in the ion drift direction.

In this paper, the island frequency is compared with drift frequencies on a database which

includes a substantial number of JET pulses in different plasma conditions, as specified in section 2. Islands with toroidal periodicity numbers from 1 to 3 are considered. The main aim of the paper is to scrutinise the possibility of exploiting measurements of island frequency to diagnose $q = m/n$ locations. The processing of magnetic signals to extract frequencies and toroidal periodicities is outlined in section **3**. Rational-q locations are determined by matching the island frequency against plasma rotation profiles, as described in section **4**.

Results on island rotation and on the diagnosis of rational-q locations are presented in section **5**. Finally, conclusions are given in section **6**.

2. Relevant diagnostics and plasma pulses selection

Doppler and ion diamagnetic frequencies are calculated from toroidal profiles of angular frequency (Ω) and temperature (T_C) of carbon impurity ions, as measured by charge-exchange recombination spectroscopy (CX). Electron diamagnetic rotation is obtained from electron temperature (T_e) profiles as measured by high resolution Thomson scattering (HRTS). Safety factor profiles are provided by equilibrium reconstruction including motional Stark effect measurements as constraints (MSE in short). Island frequencies and periodicity numbers are obtained from arrays of sensors that pick-up the poloidal magnetic field component, as described in the next section.

Plasma pulses were collated from JET experiments on the hybrid scenario with the ITER-like wall (ILW). Data from pulses with validated CX, MSE and HRTS data were recorded in a database comprising 353 MSE time slices from 47 pulses.

The database covers wide ranges of plasma parameters, with plasma current I_p = 1.4-2.5 MA, toroidal magnetic field B = 1.7-2.~~97~~ T, safety factor at the 95% flux surface q_{95}= 2.7-4.7, electron density 1.5-7×10^{19} m^{-3}, electron temperature 0.5-4 keV, ion temperature 0.5-5 keV (density and temperatures at the relevant rational-q locations from MSE). The range of normalized beta, defined as $\beta_N = \beta/(I_p/aB)$ with β (in %) the plasma to magnetic field pressure ratio and a (in m) the plasma minor radius, is 0.5-3.5. All the pulses were in the banana regime of collisionality.

3. Magnetic signals analysis

The available arrangements of in-vessel fast magnetic field sensors allow to detect magnetic fluctuations up to 1 MHz and to identify toroidal mode numbers up to n = 15. The frequency

range of observed tearing modes is up to 150 kHz, with toroidal numbers up to $n = 7$. The analysis can be conceptually divided into three steps, first determination of amplitude and toroidal number as a function of time and frequency, second recognition of coherent modes, third determination of markers for rational-q locations. The first two steps are autonomous and will be described in the next subsections. The third one, which involves other diagnostics and some assumptions, is described in section 4.

3.1 Amplitude and toroidal number spectrograms

Fluctuation amplitudes and toroidal numbers as a function of time and frequency are obtained by processing short (8 ms) time segments of signals from a toroidal array of six sensors with non-constant spacing. Linear processing of complex amplitudes in the frequency domain is employed [12]. An example of this step of the analysis is shown in figure 1 for JET pulse 84682, with $q_{95} = 2.9$, $\beta_N = 2.5$, $B = 2$ T and $I_p = 2.1$ MA. Several modes with different amplitude appear as evolving lines in the amplitude spectrogram (figure 1a). Toroidal numbers as obtained by fitting phase differences between coils are shown in figure 1b. The frequency span and the toroidal number selection are chosen in order to highlight modes with $n \leq 3$. Modes with toroidal number up to $n = 6$ and frequency up to 90 kHz are detected in this pulse but are not shown for clarity.

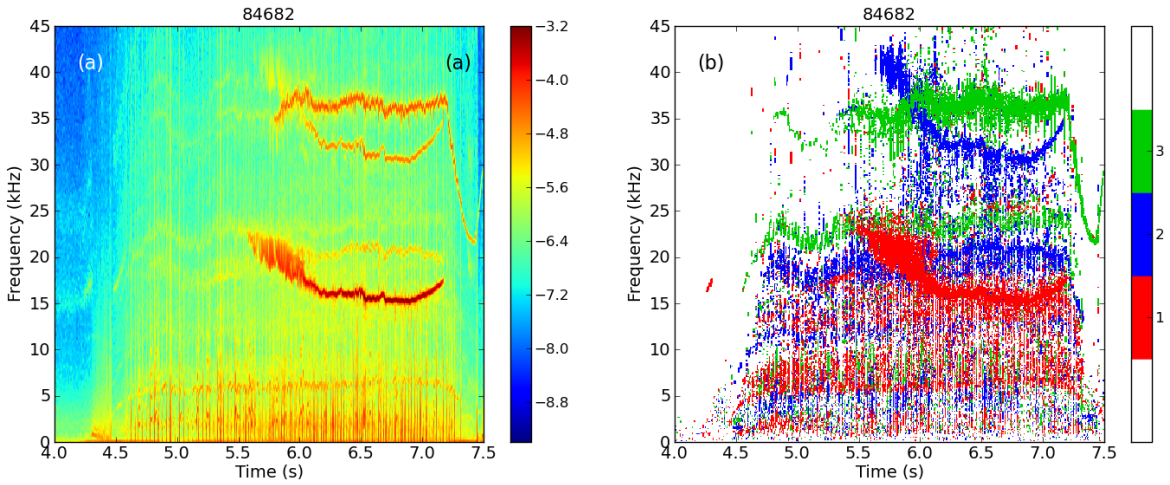

Figure 1. (a) Spectrogram of magnetic field perturbation at magnetic sensors, with colours representing the common logarithm of zero-to-peak amplitude in Tesla. (b) Spectrogram with colours representing toroidal number for pixels with logarithm of amplitude larger than -7.

3.2. Detection of coherent modes

In the second step, coherent modes are recognised as regular patterns in the spectrograms. For each toroidal number, pixels corresponding to other numbers are masked and spectral maxima in the remaining pixels are tracked along time. A threshold of 10^{-7} T is imposed on amplitude in order to minimise false detections due to noise. Overtones of strong modes are identified and discarded, for example the $n = 2$ feature at 30-35 kHz in figure 1 is discarded for being recognised as an overtone of a strong $n = 1$ mode. The two most intense detected modes (for each n) are selected for storage and further processing. From figure 2 it can be seen that, having used low thresholds, very weak and intermittent modes are detected along with strong and continuous ones. The former are usually discarded in works dealing with MHD effects on plasma performance, but their inclusion significantly extends the statistical basis for the analyses presented in section 5.

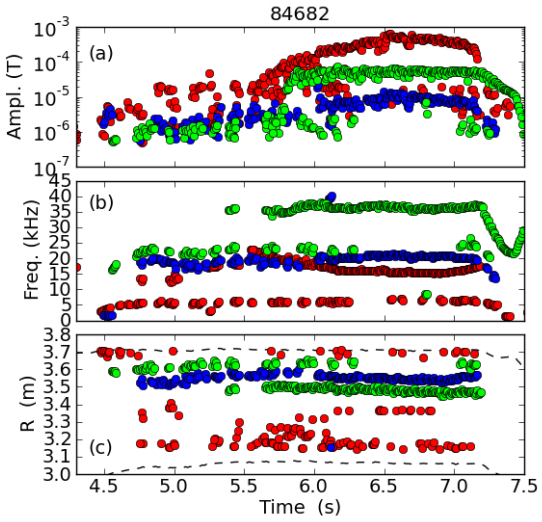

Figure 2. Coherent modes detected in pulse JET pulse 84682. (a) Poloidal field oscillation amplitude at magnetic sensors. (b) Frequency. (c) Location (as described in section 4); the upper dashed line shows the $q = 2$ radius from equilibrium reconstruction, while the lower one shows the plasma axis. Red, blue and green colours represent modes with toroidal number $n = 1, 2, 3$ respectively. Detected modes with $n > 3$ are not shown.

4. Determination of rational-q locations

In the third step of the analysis, measured frequencies are translated into radial island

locations. This step is grounded on the theoretical result that the phase velocity of tearing modes is determined by torque balance in narrow regions localised around the $\mathbf{k}\cdot\mathbf{B}=0$ surfaces, where dissipative effects are important [13] and where magnetic island chains are formed by field lines reconnection. Here $\mathbf{B}$ is the equilibrium magnetic field and $\mathbf{k}=n\nabla\zeta-m\nabla\vartheta$ is the island wavevector along the toroidal (ζ) and poloidal (ϑ) angles in flux coordinates (see appendix).

It follows that, in the absence of any electromagnetic interaction with external structures or with other island chains, the island frequency has to depend on plasma properties at the $\mathbf{k}\cdot\mathbf{B}=0$ (or equivalently $q = m/n$) surface. If such a dependence can be established in terms of measured quantities, it can be formally cast as a frequency profile, and the $q=m/n$ location can be obtained from the intersection between this profile and the measured mode frequency (see figure 3).

As stated in the introduction, theoretical studies have given island frequencies of the order of the diamagnetic frequencies, but a sufficiently complete theory is not available at present. However, for the strongly rotating plasmas that are studied in this paper, the Doppler shift contribution is dominant and then propagation in the plasma frame can be considered as a small correction, which can be approximately determined using an empirical approach. It is worth remarking that a large Doppler shift eases the diagnostic application, while it disadvantages basic studies on island propagation.

In order to determine the effect of island propagation in the plasma frame, frequencies calculated according to Tthree very simple models on island frequency in the plasma frame (namely zero frequency, $\omega_{*\mathrm{i}}$ and $\omega_{*\mathrm{e}}$) are evaluated inshifted to the laboratory frame (see appendix) and compared with measured frequencies. The Doppler shift due to the $\mathbf{E}\times\mathbf{B}$ drift is calculated from force balance of carbon impurity ions,, as detailed in the appendix, it can beunder some approximatedions as equation (1), which reduces the required diagnostic information to equilibrium, rotation and temperature profiles:

$$\omega_E = n\left(\Omega + \frac{1}{6}\frac{dT_C}{d\psi}\right) \quad , \qquad (1)$$

where Ω and T_C are respectively toroidal angular frequency and temperature (in rad/s and eV units respectively) of carbon ions, n is the toroidal mode number and ψ is poloidal magnetic flux divided by 2π.

The Doppler-shifted ion and electron diamagnetic frequencies, dubbed ion and electron

frequency in the following, are evaluated using similar approximations (see appendix),

$$\omega_i = n\left(\Omega - \frac{5}{6}\frac{dT_C}{d\psi}\right) \qquad (2)$$

and

$$\omega_e = \omega_E + n\frac{dT_e}{d\psi} \quad , \qquad (3)$$

where T_e is electron temperature in eV units.

Expressions (1-3) are used in two ways. First, expected frequencies are calculated for each model by substituting profile data interpolated at rational-q locations as given by MSE; the results are then compared with measured frequencies in order to establish which model gives the best approximation for island propagation. ~~It will be shown in section 5 that best agreement is obtained with the ion frequency model (2).~~ Second, formally regarding expressions as frequency profiles, rational-q locations are determined from the intersections with measured frequencies (see figure 3).

A systematic comparison with rational-q locations from MSE is presented in section 5, while the detailed analysis of a time slice of the spectrograms shown in figure 1 is illustrated in the rest of this section. Locations are determined in term of major radius on the low-field-side, where CX channels are placed. Model (2) is used. Five independent modes are present in the considered time slice; their frequencies are divided by the respective toroidal numbers and the model frequency profile is calculated for $n = 1$, in order to display all modes in a single frequency-matching diagram. The Ω profile is also shown to discern the temperature gradient contribution. From figure 3 it can be seen that the latter is small and regular in the outer half radius and tends to diverge towards the magnetic axis, a natural consequence of error amplification by the derivative with respect to poloidal magnetic flux, so that locations close to the magnetic axis are not reliable. Expression (2) is not evaluated at the outer point, which falls in the pedestal region, where profiles are not adequately resolved. No location is produced and an error code is generated for frequencies outside the plotted range of (2). Identified locations are marked by arrows in figure 3. No location is found for the mode that lies just above 16 kHz; anyway its location would be meaningless for two reasons, first it is too close to the axis and second, as shown by its chirping character (see figure 1), it is not a tearing mode but a fishbone mode [**14**], with frequency determined by precession of energetic particles and not by local torque balance.

The poloidal periodicity (m) number has not been used so far, but it is needed at this point to associate detected locations with rational-q values. The m number can not be determined from magnetic signals, because the layout of sensors is not adequate to resolve shaping effects. An indirect determination can however be done, provided that the safety factor profile is monotonic and that the $q = 2$ radius is sufficiently external to be reasonably well approximated by equilibrium reconstruction even without MSE additional constraints. This is the case for both hybrid and baseline plasma scenarios, while the indirect determination fails in advanced scenarios. The $n = 1$ mode at lower frequency is identified as $(m, n) = (2, 1)$ for being located close to the $q = 2$ proxy given by equilibrium reconstruction. The $n = 2$ mode is identified as (3, 2) for being more internal than the $q = 2$ proxy. The $n = 1$ mode at higher frequency must have $m = 1$, confirming its fishbone nature. As for the pair of $n = 3$ modes, the most internal must have $m = 4$ and the other one $m = 5$. The time history of rational-q locations is shown in figure 2c. (3, 2) and (4, 3) modes form continuous lines, while detection of other modes is sporadic. Locations of the (1, 1) mode (red dots at $R < 3.5$) are not meaningful, as discussed above.

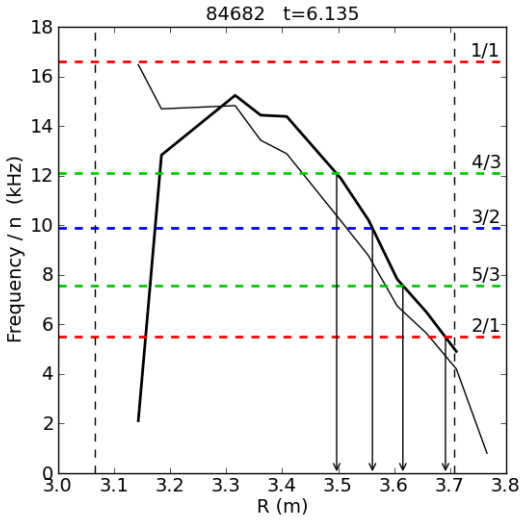

Figure 3. Frequency-matching diagram. The thick solid line shows expression (2) calculated for $n = 1$ and the thin one shows the toroidal angular frequency profile; both are rescaled from rad/s to kHz. Horizontal dashed lines show mode frequencies divided by n. Red, blue and green indicate $n = 1$, 2 and 3 respectively. The identified (m, n) pairs are annotated. The outer (inner) vertical dashed line shows the $q = 2$ radius (the plasma axis) from equilibrium reconstruction. Locations resulting from frequency matching are indicated by vertical arrows.

5. Statistical analysis of mode frequencies and rational-q locations

The statistical comparison between measured and predicted frequencies is used to establish which one of expressions (1) - (3) gives the best model for island rotation. Frequencies are given in kHz (and not rad/s) units for consistency with spectrograms. Measured, Doppler, ion and electron frequencies are indicated by f_{MHD}, F_E, F_i, and F_e respectively. The comparison is done for (2, 1) modes in the next subsection. The statistical analysis of frequencies is illustrated by scatter plots and by histograms. The former provide a glance at the frequency span covered by the database and help identifying the nature of outliers, but, since many data points overlap, statistical information has to rely on histograms. For each MSE time slice, mode frequencies and locations falling within 0.1 s from the MSE time are considered. There are possibly many data points in each time interval, about 20 on average.

A by-product of this analysis is the determination of the sign and of the approximate value of island frequency in the plasma frame. Subsequently, rational-q locations obtained using the selected model are systematically compared with MSE results, in order to evaluate the diagnostic potential in quantitative terms.

5.1 n = 1 modes

Central $n = 1$, $m = 1$ MHD modes, in the form of fishbones or sawtooth precursors or continuous tearing modes [15] are detected in almost all the pulses included in the database. Their frequency roughly corresponds to the maximum of the toroidal rotation profile, but a quantitative comparison with island rotation models is precluded by large errors that affect the temperature gradient in the central region, as discussed in section 4.

Other $n = 1$ modes at lower frequency (less than half typically) are identified as $m = 2$ tearing modes for having location close to the $q = 2$ radius as given by MSE. The amplitude of these modes is small, below 2×10^{-5} T poloidal field perturbation at magnetic sensors, corresponding to island widths of around 1.5 cm; a strong $m = 2$ mode with 2×10^{-3} T amplitude is present in one pulse only.

The scatter plot of measured frequencies (f_{MHD}) versus $F_i(n = 1, q = 2)$, i.e. the ion frequency from expression (2) calculated for $n = 1$ at the $q = 2$ radius from MSE, is shown in figure 4. Use of other model frequencies would give qualitatively similar plots. A few points above 30 kHz are left out of figure 4 but are included in figure 5.

Most data points populate two diagonal bands, one bunching around the identity line and the

other with higher inclination. Points in the upper band most likely correspond to central $m = 1$ modes, in fact inspection of spectrograms for a number of cases shows that the corresponding spectral features are either fishbones or sawtooth precursors. Points clumped around the identity line are most likely originated by $m = 2$ tearing modes. As for points lying well below the identity line, some ones can be identified as $m > 2$ modes as they coexist with with clear $m = 2$ modes lying at higher frequency; however, no case-by-case cleaning has been done, so all these points will remain as tails in the following statistics.

Markers in red (blue) indicate frequencies that lie below (above) $F_i(n = 1, q = 1.5)$, i.e. the ion frequency calculated for $n = 1$ at the $q = 1.5$ radius. Use of F_E or F_e would nearly give the same subsets, because the separation between $m = 1$ and $m = 2$ mode frequencies in each pulse is much larger than the differences between the three models. The comparison with calculated frequency at $q = 1.5$ could be used to automatically discriminate between $m = 1$ and $m = 2$ modes, but here the colour code is only intended to ease the comparison between scatter plots and histograms.

The histogram of $f_{MHD} / F_i(n = 1, q = 2)$ is shown in figure **5.** The colour code of figure **4** is preserved by using semi-transparent histogram bars. Data points marked in red, which are most likely due to $m = 2$ modes, form a well-defined peak around identity. The peak is sufficiently narrow to allow comparing different island rotation models, as detailed below. Data points marked in blue (likely due to $m = 1$ modes) populate a broad feature between 1.5 and 3 frequency ratio, which comprises a large number of counts because the $m = 1$ mode is present in almost all pulses. There is no reason to expect a narrow peak for this subset, in fact the normalisation frequency is evaluated far from the $q = 1$ radius; furthermore, $m = 1$ modes in the form of fishbones have intrinsically broad frequency range.

Different island rotation models are compared in figure **6**. Panel (a) reproduces f_{MHD} / F_i, i.e. data normalised to the ion frequency from (2), like in figure **5**. It can be seen that when using f_{MHD} / F_E, i.e. the Doppler frequency from (1), panel (b), and f_{MHD} / F_e, the electron frequency from (3), panel (c), the peak progressively shifts away from identity and becomes broader. It can be concluded that the ion frequency from (2) gives the best model for the determination of rational-q locations. Results of normal distribution fits to the peak (also shown in figure **6**) are given in Table 1.

As remarked previously, differences between the three models are relatively small because of the large value of the common Doppler shift; on the one hand this eases the diagnostic

application, but on the other hand, it increases the uncertainty on island propagation in the plasma frame. However, the sign and the order of magnitude of the latter can be determined: Doppler shift subtraction and normalisation to the ion diamagnetic frequency gives an average value of 0.8, i.e. the sign corresponds to the ion drift direction, and the value is comparable with the ion diamagnetic frequency. An average value of 0.5 was found in [4] for the (2, 1) mode.

Table 1. Statistics of the comparison between different island rotation models

model	mean	standard deviation
f_{MHD} / F_i	0.985	0.08
f_{MHD} / F_E	1.083	0.09
f_{MHD} / F_e	1.190	0.12

Turning now to the comparison between $q = 2$ locations from MSE and the ones from mode frequency matching with ion fluid rotation from (2), the histogram of differences between locations is shown in figure 7, with the same colour code as in previous figures.

The peak appearing around identity in figure 5 transforms into a peak around zero deviation between locations. Locations are not produced for data points that populate the tail at low values of f_{MHD} / F_i (and are most likely associated with $m > 2$ modes), because the corresponding frequencies fall in the discarded pedestal region (see discussion on figure 3). The normal distribution fit shown in figure 7 has a mean of 0.015 m and a standard deviation of 0.032 m. Giving some margin to these values in order to account for the skewness of the actual distribution, it can be concluded that, as a result of errors in CX and MSE diagnostics and of the approximations used in the model, the systematic deviation of $q = 2$ locations from mode frequency matching is about 2 cm and the error bar to one standard deviation is about 4 cm.

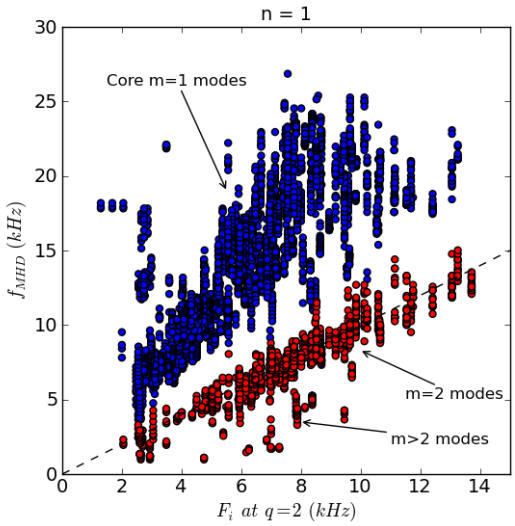

Figure 4. Measured frequencies of $n = 1$ modes versus the ion frequency as calculated from (2) for $n = 1$ at the $q = 2$ radius and rescaled in kHz. Data points with frequency above the ion frequency at $q = 1.5$, which most likely correspond to core $m = 1$ modes, are marked in blue. The other points (in red) likely correspond to poloidal numbers $m \geq 2$. The dashed line represents identity. Likely poloidal numbers are annotated.

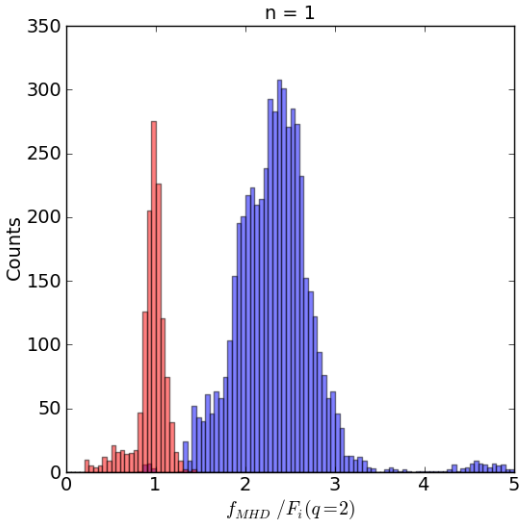

Figure 5. Distribution of the ratio between measured frequency of $n = 1$ modes and the ion frequency calculated from (2) for $n = 1$ at the $q = 2$ radius. Bars in red (blue) are formed by data points marked with the same colours in figure 4.

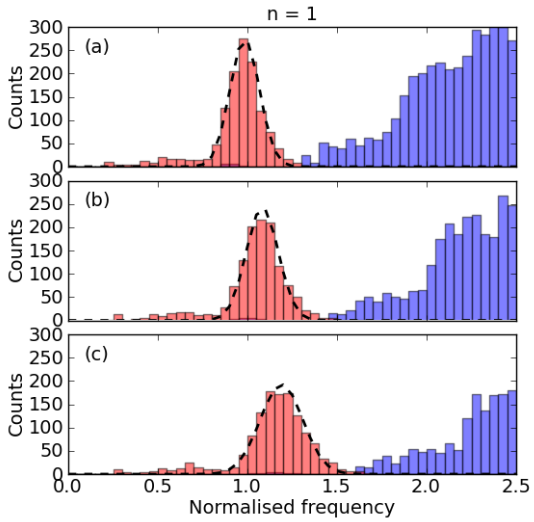

Figure 6. Distributions of the ratio between measured frequency of $n = 1$ modes and different frequencies calculated for $n = 1$ at the $q = 2$ radius. (a) Ion frequency from (2). (b) **E**×**B** drift frequency from (1). (c) Electron frequency from (3). Bars in red (blue) are formed by data points marked with the same colours in figure 4. Overlaid curves show scaled normal distributions.

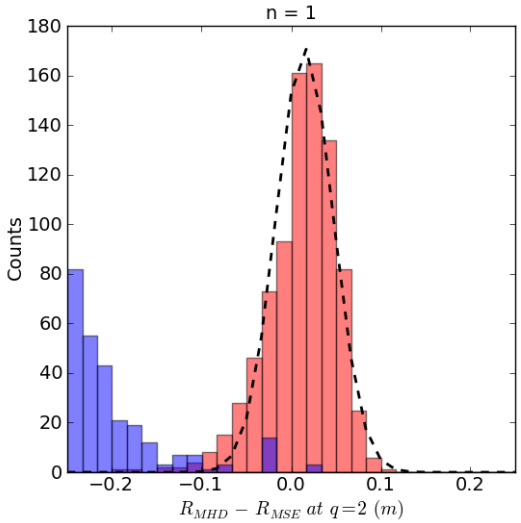

Figure 7. Distribution of deviations between $q = 2$ locations from mode frequency and from MSE. Bars in red (blue) are formed by data points marked with the same colours in figure 4. The overlaid curve shows a scaled normal distribution with 0.015 m mean and 0.032 m standard deviation.

5.2. $n = 2$ modes

Modes with $n = 2$ toroidal number are detected in the majority of pulses of the database. Amplitudes are distributed in a wide range; in the following, $n = 2$ modes are classified as strong if the poloidal field perturbation at sensors is above 3×10^{-5} T, which correspond to about 3 cm island width.

The scatter plot of measured frequencies (f_{MHD}) versus $F_i(n = 2, q = 1.5)$, i.e. the ion frequency from expression (2), calculated for $n = 2$ at the $q = 1.5$ radius from MSE, is shown in figure **8**. Markers in blue (red) indicate frequencies higher (lower) than $F_i(n = 2, q = 2)$, i.e. expression (2) evaluated for $n = 2$ at the $q = 2$ radius; points in red colour likely correspond to modes with $m \geq 5$.

It can be seen that $n = 2$ mode frequencies are roughly distributed in four groups. The majority bunching around identity is most likely constituted by $m = 3$ modes. Outliers at high frequency (second group) are due to $n = 2$, $m = 2$ overtones of strong $n = 1$ fishbone modes (overtones are suppressed in most cases, but a little leakage persists). The third group, i.e. red circles at moderately low frequency, can be attributed to $m = 5$, $n = 2$ modes for being below the expected frequency at the $q = 2$ radius. Outliers below 15 kHz are likely edge modes with even higher m.

The histogram of $f_{MHD} / F_i(n = 2, q = 1.5)$ is shown in figure **9.** The colour code of figure **8** is preserved by using semi-transparent bars. The peak formed by likely $m = 3$ modes is slightly shifted above identity. A normal distribution fit to the main peak, also shown in the figure, gives 1.087 mean and 0.105 standard deviation. Even larger shifts result when normalising measured frequencies to F_E or to F_e. The analysis in the plasma frame, performed subtracting the Doppler shift from measured frequencies and dividing by the ion diamagnetic frequency like in [**4**], results in an average ratio of 1.8, while the result found in [**4**] for the (3, 2) mode was about unity. From figure **10** it can be seen that mode amplitude has some influence on the shift, in fact weak modes, which are represented by bars in pale colour, have smaller shift. The larger shift of strong modes can not be attributed to braking by interaction with error fields, which would give the opposite effect. Meanwhile, acceleration by non-linear interaction with central $n = 1$ modes would give the right trend.

The histogram of differences between $q = 1.5$ locations from MSE and from mode frequency matching with ion fluid rotation from (2) is shown in figure **11**. Bars in pale colour highlight weak modes. The histogram features a main peak around zero and a smaller lobe between -0.1

and -0.2 m. The lobe is not related to secondary features that appear in frequency ratio histograms, instead it is originated by data points lying in the right side of the main peak. Neither high-frequency outliers originated by overtones, nor low-frequency points that are likely due to $m \geq 5$ modes contribute to this histogram, since they lie outside the extremes of the frequency profile to be matched and then produce no location data (see discussion on figure 3).

A normal distribution fit to the main peak (also shown in figure **11**) gives a mean of -0.016 m and a standard deviation of 0.038 m. Even better figures would result when discarding strong modes. However, the presence of the lobe, i.e. the possibility of errors up to 0.2 m is a problem for the diagnostic application. Inspection of frequency-matching diagrams reveals that profiles from (2) have particularly low gradient in these cases. The problem can then be overcome by rejecting locations if the slope of the frequency profile is below a threshold value, but this practical implementation is outside the scope of this paper.

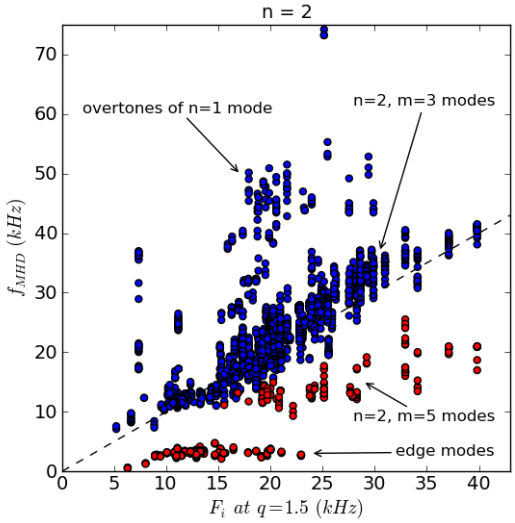

Figure 8. Measured frequencies of $n = 2$ modes versus the ion frequency as calculated from (2) for $n = 2$ at the $q = 1.5$ radius and rescaled in kHz. Data points with frequency above the ion frequency at $q = 2$, which most likely correspond to $m = 3$ modes (exceping overtones), are marked in blue. The other points (in red) likely correspond to poloidal numbers $m \geq 5$. The dashed line represents identity.

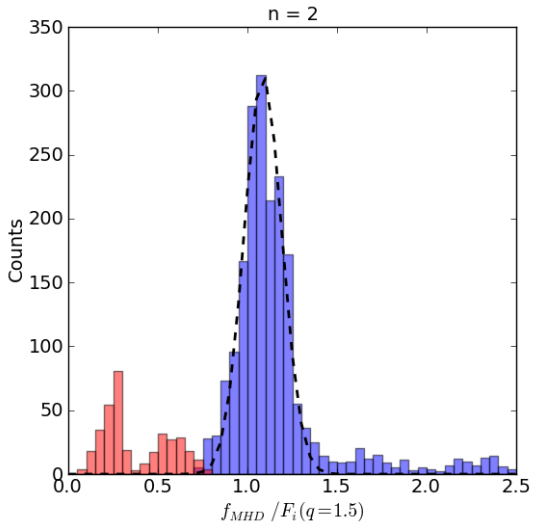

Figure 9. Distribution of the measured frequency of $n = 2$ modes normalised to the ion frequency calculated from (2) for $n = 2$ at the $q = 1.5$ radius. Bars in blue (red) are formed by data points marked with the same colours in figure 8. The overlaid curve shows a scaled normal distribution with a mean of 1.087 and a standard deviation of 0.105.

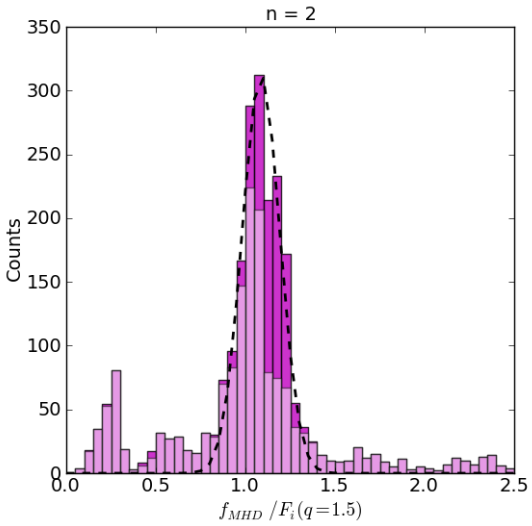

Figure 10. Distribution of the ratio between measured frequency of $n = 2$ modes and the ion frequency calculated from (2) for $n = 2$ at the $q = 1.5$ radius. Bars in dark colour represent all $n = 2$ modes; bars in pale colour show modes with amplitude below 3×10^{-5} T. The overlaid curve shows a scaled normal distribution with 1.087 mean and 0.105 standard deviation (same as in figure 9).

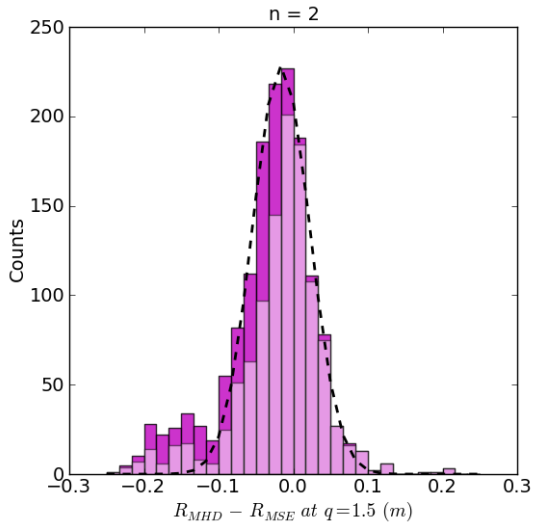

Figure 11. Distribution of deviations between $q = 1.5$ locations from mode frequency and from MSE. Bars in dark colour represent all $n = 2$ modes. Bars in pale colour show modes with amplitude below 3×10^{-5} T. The overlaid curve shows a scaled normal distribution with -0.016 m mean and 0.038 m standard deviation.

5.3. $n = 3$ modes

The difficulty of resolving the m-number ambiguity increases with toroidal number, because the distance between rational-q surfaces, and then the frequency separation, gets smaller. In the $n = 3$ case, both the $m = 4$ and the $m = 5$ resonances fall in the plasma core and form partially overlapped frequency and location distributions.

The scatter plot of measured frequencies (f_{MHD}) versus $F_i(n = 3, q = 4/3)$, i.e. the ion frequency from model (2), calculated for $n = 3$ at the $q = 4/3$ radius from MSE, is shown in figure **12**. Data are divided in two subsets, one with frequencies higher than $F_i(n = 3, q = 1.5)$, i.e. expression (2) evaluated for $n = 3$ at the $q = 1.5$ radius, marked in blue, and the complementary one (marked in red). The first subset and the second one are assumed to be constituted by $m = 4$ and $m \geq 5$ modes respectively The distinction in two subsets is used here to resolve the overlap of distributions, whereas in previous subsections it was only intended to assign colour codes to help comparing different plots.

The histogram of $f_{MHD} / F_i(n = 3, q = 4/3)$ is shown in figure **13.** The colour code of figure **12** is preserved by using semi-transparent histogram bars. Points (marked in blue) that most likely correspond to $m = 4$ modes form a well-defined peak, which is shifted from unity by about 10%. A normal distribution fit gives 1.087 mean and 0.1 standard deviation. Larger

shifts result when normalising neasured frequencies to F_E or to F_e. The analysis in the plasma frame, performed subtracting the Doppler shift from measured frequencies and dividing by the ion diamagnetic frequency like in [4], results in an average ratio of 1.8, while the result found in [4] for the (4, 3) mode was about 1.7.

When considering $f_{MHD} / F_i(n = 3, q = 5/3)$, i.e. the measured frequency normalised to the ion one at $q = 5/3$, some structure emerges for points marked in red, which most likely correspond to $m \geq 5$ modes, while the $m = 4$ peak becomes much broader. figure **14** it can be seen that a peak around identity appears, which can be associated with $m = 5$ modes, while counts lying below 0.7 frequency ratio are most likely due to modes with $m > 5$.

The histogram of differences between $q = 4/3$ locations from MSE and from mode frequency matching is shown in figure **15**. Data identified as corresponding to $m = 4$ form a non-gaussian peak (featuring long wings) with maximum at 0.023 m, a mean of 0.028 m and a standard deviation of 0.056 m.

Locations of $q = 5/3$ from MSE and from mode frequency matching are compared in figure **16**. Data identified as corresponding to $m = 5$ form a non-gaussian peak (featuring short wings) with mean at 0.005 m and standard deviation of 0.043 m. Data with low normalised frequency (below 0.7 in figure **14**) do not appear in location histograms because they fall below the minimum of the frequency profile to be matched.

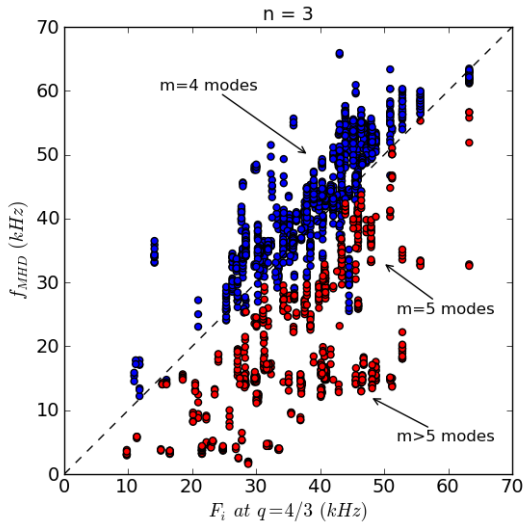

Figure 12. Measured frequencies of n = 3 modes versus the ion frequency calculated from (2) for n = 3 at the q = 4/3 radius and rescaled in kHz. Data points with frequency above (below) the ion frequency at q = 1.5 are marked in blue (red). Likely poloidal numbers are annotated. The dashed line represents identity.

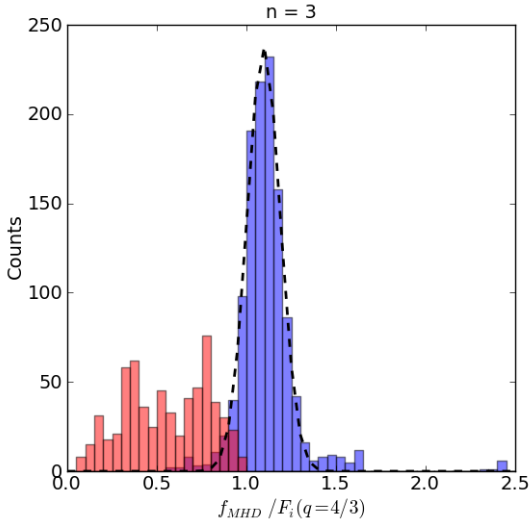

Figure 13. Distribution of the ratio between measured frequency of n = 3 modes and the ion frequency calculated from (2) for n = 3 at the q = 4/3 radius. Bars in blue (red) are formed by data points marked with the same colours in figure 12. The overlaid curve shows a scaled normal distribution with a mean of 1.087 and a standard deviation of 0.1.

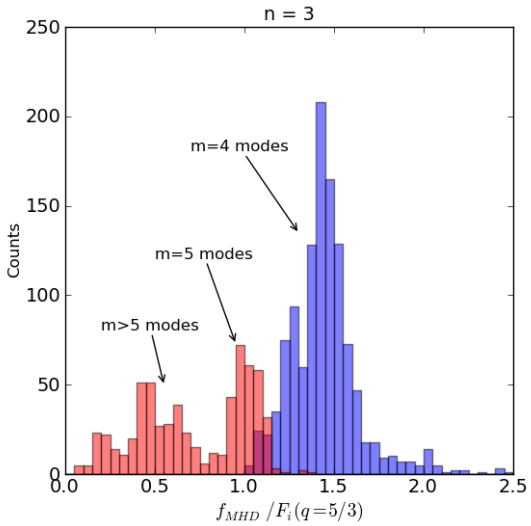

Figure 14. Distribution of the ratio between measured frequency of $n = 3$ modes and the ion frequency calculated from (2) for $n = 3$ at the $q = 5/3$ radius. Bars in blue (red) are formed by data points marked with the same colours in figure 12. Likely poloidal numbers are annotated.

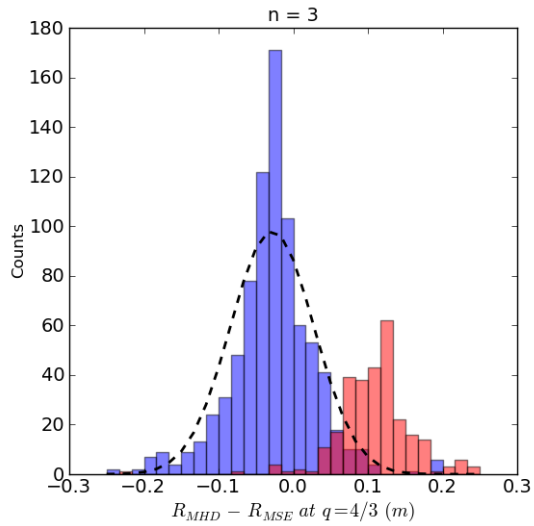

Figure 15. Distribution of deviations between $q = 4/3$ locations from mode frequency and from MSE. Bars in blue (red) Bars in blue (red) are formed by data points marked with the same colours in figure 12. The overlaid curve shows a scaled normal distribution having the same mean and the same standard deviation as points marked in blue.

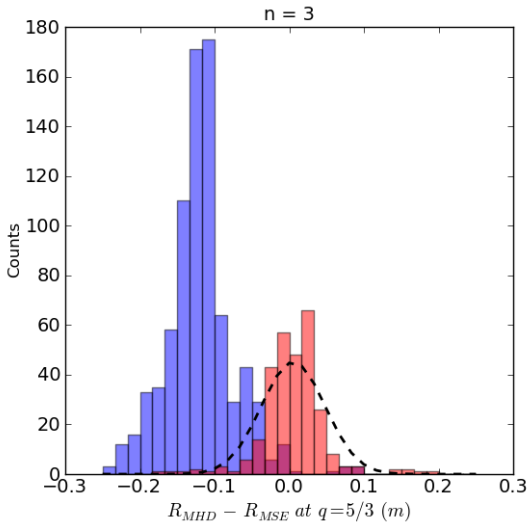

Figure 16. Distribution of deviations between $q = 5/3$ locations from mode frequency and from MSE. Bars in blue (red) are formed by data points marked with the same colours as in figure 12. The overlaid curve shows a scaled normal distribution having the same mean and the same standard deviation as points marked in red.

6. Conclusions

The propagation of magnetic islands in JET has been examined, in view of its exploitation to diagnose locations of $q = m/n$ rational surface locations from the frequency of magnetic signals produced by islands with poloidal number m and toroidal number n. Statistical analysis of a database including many well-diagnosed plasma pulses has been done. Island propagation in the plasma frame, i.e. with subtracted $\mathbf{E}\times\mathbf{B}$ Doppler shift, results to be definitely in the ion diamagnetic drift direction, in agreement with results in [4], with values ranging from 0.8 (for islands at the $q = 2$ resonant surface) to 1.8 (for more internal islands) times the ion diamagnetic frequency. The diagnostic potential of the assumption of propagation at the ion diamagnetic frequency has been scrutinised. Frequency profiles to be matched against measured frequencies have been calculated neglecting poloidal plasma rotation, density gradients and electromagnetic torques between the island chain and other islands or external error fields. It is worth remarking that these approximations are reasonable if the plasma rotation frequency is much larger than the diamagnetic frequency, as discussed in the appendix, whereas more accurate estimates of island rotation in the plasma frame would be required for plasmas with slower toroidal rotation.

The rational-q locations resulting from frequency matching have been compared with the ones measured by equilibrium reconstruction including motional Stark effect measurements as constraints. Systematic shifts and standard deviations that result from this analysis are shown in table **2**. The resulting deviations are rather small, in spite of the rough assumption that have been done on island propagation and of the intrinsic uncertainties of diagnostics involved in the comparison.

Some useful diagnostic applications can be envisaged on the basis of these results. The presence of tearing modes (not necessarily strong ones) is obviously a prerequisite that limits the scope of these applications to particular plasma scenarios, such as hybrid and advanced ones. The first application is to check the overall reliability of MSE and CX data by comparing rational-q locations. Second, the evolution of rational-q locations can be followed with high time resolution. Third, the poloidal number of instabilities can be determined, at least for modes with $n < 3$, even in the absence of complete poloidal arrays of magnetic sensors. Fourth, constraints for equilibrium reconstruction can be supplied in the absence of MSE data.

Table 2. Statistics of the shift between rational-q location from mode frequency and from MSE

mode	mean	standard deviation
2/1	1.5 cm	3.9 cm
3/2	-1.6 cm	3.8 cm
4/3	-2.8 cm	5.6 cm
5/3	0.5 cm	4.3cm

Appendix

A perturbation which reconnects field lines at the $q(\psi_s)=m/n\equiv q_s$ rational surface has the generic form $f(\psi,\ n\zeta-m\vartheta)$ [16], where symmetry flux coordinates [17] are used, namely ψ is the flux surface label (i.e. poloidal magnetic flux divided by 2π), ϑ is the straight field-lines poloidal coordinate and ζ is the toroidal angle. In these coordinates

$$\mathbf{B}=q(\psi)\nabla\psi\times\nabla\vartheta-\nabla\psi\times\nabla\zeta \qquad \text{(A1)}$$

and the Jacobian in terms of major radius and toroidal field is qR/B_T .

The perturbation is periodic in the angular variable, $f(\psi,\alpha+2\pi)=f(\psi,\alpha)$. A propagating perturbation will be time-dependent according to $f(\psi,n(\zeta-v^{\zeta}t)-m(\vartheta-v^{\vartheta}t))$, where $v^{\vartheta}=\mathbf{v}\cdot\nabla\vartheta$ and $v^{\zeta}=\mathbf{v}\cdot\nabla\zeta$ are contravariant components of the propagation velocity at the $q=q_s$ surace (and $v^{\psi}=0$ in cases of interest). Defining

$$\mathbf{k}=n\nabla\zeta-m\nabla\vartheta \ , \qquad \text{(A2)}$$

the time-dependence takes the form $f(\psi,\ n\zeta-m\vartheta-\mathbf{k}\cdot\mathbf{v}\,t)$. Owing to periodicity, the spectrum will be composed by the $\mathbf{k}\cdot\mathbf{v}$ frequency and by its harmonics. Expressions for the frequencies introduced in section 4 are now worked out.

The diamagnetic velocity for a species j is

$$\mathbf{V}_{*j}=\frac{1}{e_j n_j B^2}\mathbf{B}\times\nabla p_j=\frac{p'_j}{e_j n_j B^2}\mathbf{B}\times\nabla\psi \ ,$$

where the notation $f'=\mathrm{d}f/\mathrm{d}\psi$ is used.

Since, from (A1) and (A2), $\mathbf{k}\times\nabla\psi=n\mathbf{B}$ at the $q=q_s$ surface, the diamagnetic frequency $\omega_{*j}=\mathbf{k}\cdot\mathbf{V}_{*j}$ takes the simple form

$$\omega_{*j}=-n\,p'_j/(e_j n_j) \ . \qquad \text{(A3)}$$

The Doppler shift $\omega_E=\mathbf{k}\cdot\mathbf{E}\times\mathbf{B}/B^2$ is evaluated from the force balance of carbon impurity

ions,

$$\mathbf{E}=\frac{1}{e_C n_C}\nabla p_C - \mathbf{V}_C \times \mathbf{B} \quad ,$$

which gives

$$\omega_E = n\Omega - \omega_{*\mathrm{C}} - m\mathbf{V}_C \cdot \nabla \vartheta \quad , \tag{A4}$$

where $\Omega = \mathbf{V}_C \cdot \nabla \zeta$ is the toroidal angular frequency of carbon ions.

The diamagnetic frequencies in the laboratory frame are

$$\omega_i = \omega_E + \omega_{*i} \tag{A5}$$

and

$$\omega_e = \omega_E + \omega_{*e} \quad . \tag{A6}$$

Evaluating expressions (A4-A6) from experimental data necessarily involves a number of assumptions. First, equal temperature is assumed for fuel and carbon ions, $T_i = T_C$. Second, density gradients are disregarded. Third, poloidal rotation of carbon ions is neglected. With these assumptions, (A4)-(A5) reduce to

$$\omega_E = n\left(\Omega + \frac{1}{6}\frac{dT_C}{d\psi}\right) \tag{A7}$$

(for fully ionised carbon ions) and

$$\omega_i = n\left(\Omega - \frac{5}{6}\frac{dT_C}{d\psi}\right) \tag{A8}$$

while the electron frequency becomes

$$\omega_e = \omega_E + n\frac{dT_e}{d\psi} \quad , \tag{A9}$$

with temperatures in eV units. The temperature gradient term in (A8) is smaller than the toroidal rotation term, their ratio being 8% on average. The effect of disregarding density gradients can be estimated for the electron frequency using the electron density profile from HRTS. The density gradient contribution to the electron diamagnetic frequency changes the results of (A9) by less than 4% on average.

The effect of neglecting the last term in (A4) can be evaluated using the neoclassical expression for carbon poloidal rotation [**18**],

$$\mathbf{V}_C \cdot \nabla \vartheta = \frac{B_T^2}{q\langle B^2\rangle}\left(\frac{p'_C}{e_C n_C} - \frac{p'_i}{e n_i} + K T'_i\right) \tag{A10}$$

where angle brackets indicate flux surface average and K is about 1.3 in the banana regime.

The inclusion of this term results in a slight upshift of the ion frequency, essentially the 5/6 factor in (A8) is replaced by K and the ion frequency increases by 4% on average.

References

[1] Karimabadi H. *et al* 2013 *Phys. Plasmas* **20** 012303

[2] Schep T.J, Pegoraro F., Kuvshinov B.N. 1994 *Phys. Plasmas* **1** 2843

[3] Smolyakov A.I. *et al* 1995 *Phys. Plasmas* **2** 1581

[4] La Haye R.J. *et al* 2003 *Phys. Plasmas* **10** 3644

[5] Alper B. *et al* 2009 *Proc. 36th EPS Conf. on Plasma Physics (Sofia, Bulgaria, 2009)* P5.169 http://epsppd.epfl.ch/Sofia/pdf/P5_169.pdf

[6] La Haye R.J. 2010 *Phys. Plasmas* **17** 056110

[7] Waelbroeck F.L. 2009 *Nucl. Fusion* **49** 104025

[8] Waelbroeck F.L. 2005 *Phys. Rev. Lett.* **95** 035002

[9] Fitzpatrick R. and Waelbroeck F.L. 2008 *Phys. Plasmas* **15** 012502

[10] Fitzpatrick R. and Waelbroeck F.L. 2009 *Phys. Plasmas* **16** 072507

[11] Buratti P. *et al* 2014 *Proc. 41st EPS Conf. on Plasma Physics (Berlin, Germany, 2014)* P1.014 http://ocs.ciemat.es/EPS2014PAP/pdf/P1.014.pdf

[12] Giovannozzi E. *et al* 2014 *Proc. 41st EPS Conf. on Plasma Physics (Berlin, Germany, 2014)* P1.015 http://ocs.ciemat.es/EPS2014PAP/pdf/P1.015.pdf

[13] Fitzpatrick R. 1993 *Nucl. Fusion* **10** 1533

[14] Chen L., White R.B. and Rosenbluth M.N. 1984 *Phys. Rev. Lett.* **52** 1122

[15] Baruzzo M. *et al* 2013 *Proc. 40th EPS Conf. on Plasma Physics (Espoo, Finland, 2013)* P5.161 http://ocs.ciemat.es/EPS2013PAP/pdf/P5.161.pdf

[16] Hazeltine R.D., Meiss J.D., *Plasma Confinement* (Addison-Wesley, Redwood City, CA, 1992)

[17] D'haeseleer W.D. et al, *Flux Coordinates and Magnetic Field Structure* (Springer-Verlag, Berlin 1991)

[18] Kim Y.B., Diamond P.H., Groebner R.J., 1991 *Phys. Fluids* **B3** 2050

Acknowledgments. *This work has been carried out within the framework of the EUROfusion Consortium and has received funding from the Euratom research and training programme 2014-2018 under grant agreement No 633053. The views and opinions expressed herein do not necessarily reflect those of the European Commission.*